CrossMark

ARTICLE

Synthesis and luminescence of $Sr_2Ta_2O_7:Pr^{3+}$: a novel blue emission, long persistent phosphor

Feihong Xue, Yihua Hu,[a] Li Chen, Guifang Ju, and Qi Zhang
School of Physics and Optoelectronic Engineering, Guangdong University of Technology, Guangzhou 510006, People's Republic of China

(Received 28 April 2016; accepted 17 October 2016)

In this paper, a novel afterglow phosphor based on praseodymium ion doped $Sr_2Ta_2O_7$ was synthesized successfully by solid-state reaction in the ambient atmosphere. The photoluminescence, afterglow, afterglow decay, and thermoluminescence (TL) properties were investigated in detail. The dependence of photoluminescence properties and long afterglow (LAG) performances on Pr^{3+} contents were investigated systematically. The optimal concentrations of Pr^{3+} ions for the best photoluminescence and LAG properties were experimentally to be 2 mol% and 0.5 mol%, respectively. Pr^{3+} exhibits prominent red emission in most reports, which derives from the $^1D_2 \rightarrow {}^3H_4$ transition. However, the predominant blue emission locating at ~489 and ~507 nm coming from $^3P_{0,1} \rightarrow {}^3H_4$ transitions were observed in praseodymium ion-doped $Sr_2Ta_2O_7$. Based on TL measurements, the trapping and de-trapping processes of charge carriers between shallower and deep traps were illustrated. A model was proposed on the basis of experimental results to explain the mechanisms of photoluminescence and LAG.

I. INTRODUCTION

Recently, long persistent phosphors (LPP) have attracted a lot of attention due to their interesting optical phenomenon that can emit light for a long time after removal of the excitation source.[1–3] Such a unique phenomenon possesses many advantages such as energy saving, environmentally friendly, and recyclable; therefore, it can be widely applied in various fields, such as but not limited to, decoration, emergency signs, traffic signs, emergency exit indicators, low level lighting, imaging storage, detection of high energy rays, etc.[4–9] Generally, emitter and trap are the most important functional centers in LPP. Traps are produced by the defects in the doping and synthesis process, usually do not emit radiation by themselves, instead they store excitation energy which can be gradually released under thermal or other physical stimulations and then be transferred to the emitters. Emitters are mostly rare earth ions or transition metals ions such as Pr^{3+}, Tb^{3+}, Eu^{3+}, Eu^{2+}, Sm^{3+}, Dy^{3+}, Ce^{3+}, Mn^{2+}, and Cr^{3+}, etc.,[10–12] which are capable of emitting radiation after being excited. Herein, Pr^{3+} ions, which can produce light emitting or long afterglow (LAG) via f–f transition in the blue, green, red regions depending on the crystal lattice of hosts for luminescence materials, were chosen as the luminescence activators for LPP in this work.

With the exploration of luminescent materials, more and more matrixes have been reported, consisting of silicates, aluminum, stannates, borates, phosphates, titanates, sufides, molybdates, tungstate, and vanadates etc.[13–16] But there are few related reports about tantalite. The tantalite compound is currently playing an important role in the field of photocatalysis, where it is used to decompose water molecules into H_2 and O_2 molecules.[17–19] Recently, layered perovskite $Sr_2Ta_2O_7$ has attracted much attention owing to its excellent photocatalytic performance.[20,21] However, to the best of our knowledge, researches on the luminescence of $Sr_2Ta_2O_7$ have never been reported yet.

Therefore, in this paper, we are reporting the photoluminescence and LAG properties of blue emission LPP of Pr^{3+} by using $Sr_2Ta_2O_7$ as host material for our phosphor.

II. EXPERIMENTAL SECTION

A. Sample synthesis

A serial of $Sr_{2(1-x)}Ta_2O_7:xPr^{3+}$ (x = 0, 0.001, 0.0025, 0.005, 0.0075, 0.01, 0.02, 0.025, 0.03, and 0.035 mol, which were denoted as samples S0–S10, respectively) samples were synthesized via a solid-state reaction method. Initially, stoichiometry amounts of $SrCO_3$ (Aladdin, A.R), Ta_2O_5 (Aladdin, A.R), and Pr_6O_{11} (Aladdin, 99.99%) were weighed out according to the formula above, and meanwhile 3 mol% H_3BO_3 was used as flux. And then the powders were mixed thoroughly in

Contributing Editor: Winston V. Schoenfeld
[a]Address all correspondence to this author.
e-mail: huyh@gdut.edu.cn
DOI: 10.1557/jmr.2016.401

 © Materials Research Society 2016

https://doi.org/10.1557/jmr.2016.401 Published online by Cambridge University Press

an agate mortar for 1 h. After that, the homogeneous mixtures were transferred into corundum crucibles and calcined at 1250 °C for 6 h in a tube furnace under ambient atmosphere. After cooling to room temperature naturally, the as-obtained samples were ground into powder for the consequent measurements.

B. Characterization

The crystalline structures of all prepared samples were identified by means of a XD-2 x-ray diffractometer (PGENERAL, Beijing, China) with Cu K_α irradiation (λ = 1.5406 Å) at a scanning stepping of 0.02° in the 2θ ranging from 10° to 70°. The absorption spectra were measured by U-3900 Spectrophotometer (Hitachi Corporation, Tokyo, Japan). The photoluminescence excitation (PLE) and emission (PL) spectra were measured by a F-7000 Fluorescence Spectrophotometer (Hitachi Corporation) with 2.5 nm slit width and 1200 nm/min scanning rate under 400 V. The afterglow spectrum of typical sample was also measured with the Hitachi F-7000. The decay curves were obtained with a GFZF-2A single-photon counter system (CNNC Beijing Nuclear Instrument Factory, Beijing, China). A FJ427A1 thermoluminescent dosimeter (CNNC Beijing Nuclear Instrument Factory) was applied to measure the thermoluminescence (TL) glow curves. All samples to be measured in decay and TL measurements were weighed in 0.2 g and 0.005 g, respectively. Prior to the TL measurements, each sample was excited for 1 min with a low pressure mercury lamp (254 nm) followed with different delaying time in dark.

III. RESULTS AND DISCUSSION

A. Phase identification

Figure 1 shows the typical X-ray diffraction (XRD) patterns of $Sr_2Ta_2O_7$:Pr^{3+} (x = 0, 0.005) samples. Clearly, the main diffraction peaks could be exactly indexed to the phase of $Sr_2Ta_2O_7$ registered in JCPDS file No. 70-0248. No detectable impurity phases were observed in all obtained phosphors, indicating that the Pr^{3+} has been successfully incorporated into the host lattice and without significantly changing the crystal structure.

The crystal structure of $Sr_2Ta_2O_7$, shown in Fig. 2, was covered to be orthorhombic system [space group *Cmcm* (63)] with lattice constants a = 3.937 Å, b = 27.198 Å, c = 5.692 Å, V = 609.49 Å^3, and Z = 4.[22,23] As shown in Fig. 2, both the Sr^{2+} and Ta^{5+} site is coordinated with six oxygen ions. This structure is formed by SrO_6^{4-} and TaO_6^{6-} octahedron in which TaO_6 octahedron is connected by corner sharing and there are two symmetrically different sites for strontium. The ionic radii of Sr^{2+} and Ta^{5+} are 1.18 Å and 0.64 Å, respectively. The ionic radii for six-coordinated Pr^{3+} is 0.99 A. Considering the ionic radii and valence between the doped and substituted ions, the trivalent praseodymium ions replaces the divalent Sr^{2+} ions with the charge imbalance, and resulting in the generation of vacancies.

B. Absorption spectra and photoluminescence properties of undoped $Sr_2Ta_2O_7$

Figure 3(a) presents the absorption spectra of pure $Sr_2Ta_2O_7$. In the spectra of $Sr_2Ta_2O_7$, there appears a strong absorption in the wave length range of 190–300 nm. This band is due to the host absorption. The optical band gap of $Sr_2Ta_2O_7$ can be calculated according to the following equation:

$$(\alpha h\nu)^2 = A(h\nu - E_g) \quad . \tag{1}$$

In which α is absorption coefficient, A is the absorption constant, ν is the light frequency, h is Planck's constant, E_g is the optical band gap, and $h\nu$ is the photon energy. The α and ν values at the steep edges of the absorption

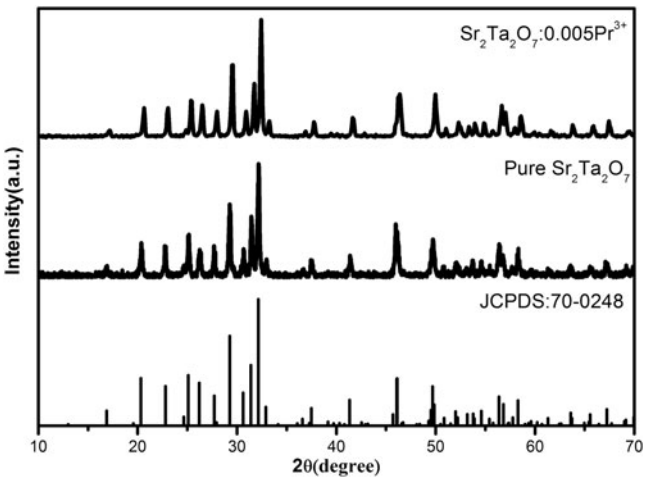


FIG. 1. XRD patterns of samples $Sr_2Ta_2O_7$ and $Sr_2Ta_2O_7$:0.005Pr^{3+}.

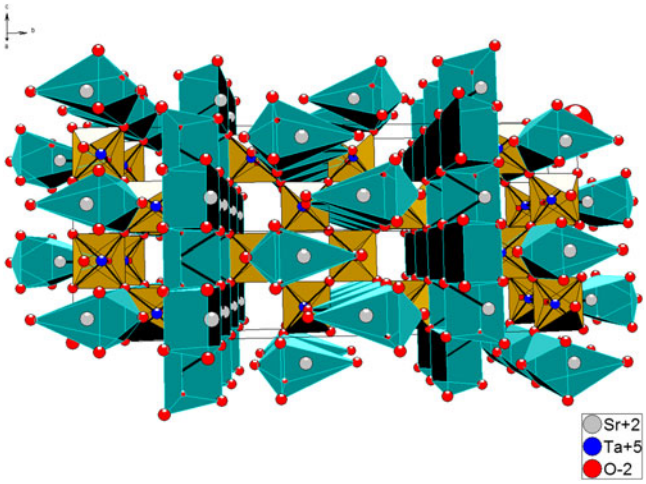


FIG. 2. The crystal structure of $Sr_2Ta_2O_7$.

https://doi.org/10.1557/jmr.2016.401 Published online by Cambridge University Press

spectra are used to construct the plots of $(\alpha h\nu)^2$ against $h\nu$. As depicted in the inset of Fig. 3(b), the curve for $Sr_2Ta_2O_7$ shows a linear region and a tangent line is drawn in the near edge region of the obtained curve. The band gaps of samples can be determined by intersection of the tangent line with the energy axis, and the value is calculated to be E_g = 4.59 eV.

Figure 4 shows the PLE (λ_{em} = 364 nm) and PL (λ_{ex} = 200 nm) spectra of undoped $Sr_2Ta_2O_7$. There can be seen a broad nonsymmetrical band range from 200 to 400 nm in the PL spectrum, which can be ascribe to the defects in host lattice. It indicates that $Sr_2Ta_2O_7$ is a self-activated luminescent matrix. The PLE spectrum was not measured completely because it is beyond the detectable wave length range of the spectrometer.

C. Luminescence properties of Pr^{3+}-doped $Sr_2Ta_2O_7$

As an example, the PLE and PL spectra of $Sr_2Ta_2O_7$:0.01Pr^{3+} are presented in Fig. 5. The PLE spectra exhibit a broad band ranging from 200 to 300 nm peak at 260 nm which is attributed to the 4*f*–5*d* transition of Pr^{3+} when monitoring emission at 486 nm. Another is in the wave length range of 420–440 nm with a very weak sharp peak which is due to the 4*f*–4*f* transitions in Pr^{3+}. When excited by 260 nm, it is obvious that the emission spectrum is composed of a weak broad band in the wave length range of 300–400 nm and several stronger sharp peaks between 450 and 700 nm. It is evident that the weak broad band ultraviolet emission is in agreement with the $Sr_2Ta_2O_7$ host emission mentioned above. While several sharp emission peaks can be observed which are attributed to the characteristic 4*f*–4*f* transitions of Pr^{3+}. The blue spectral lines observed at 486 and 498 nm are attributed to two manifolds of $^3P_0$–$^3H_4$ level,[24] which can be ascribed to the crystal field interaction. The green emission is observed at range from 500 nm to 578 nm, which are assigned to $^3P_1$–$^3H_4$ and $^3P_0 \rightarrow {}^3H_5$ transitions, respectively. The peak at ~507 is assigned to ^{3}P1–$^3H_4$ transition, while those at 533, 547, and 566 nm are attributed to three manifolds of $^3P_0$–$^3H_5$ level. The red emission lines observed at 594, 608, 630, and 657 nm can be designated to transitions of $^3P_1$–$^3H_6$, $^1D_2$–$^3H_4$, $^3P_0$–$^3H_6$, and $^3P_0$–$^3F_2$, respectively. Apparently, the blue emission from the $^3P_0$–$^3H_4$ transition is glowing brighter than the red emission from $^1D_2$–$^3H_4$, $^3P_0$–$^3H_6$, and $^3P_0$–$^3F_2$ transitions.

Figure 6 depicts the PL (λ_{ex} = 260 nm) spectra of the $Sr_2Ta_2O_7$:xPr^{3+} phosphors with different concentrations of Pr^{3+} (ranging from 0.001 to 0.035) at room temperature. As presented in Fig. 6, the emission spectra of all samples have no obvious changes in the spectral configuration except for the emission intensity. As shown in the inset, it is noticeable that the PL intensity of $Sr_2Ta_2O_7$:xPr^{3+} reaches a saturation point at x = 0.02 mol. After that, the PL intensity begins to decline dramatically owing to the concentration quenching effect.

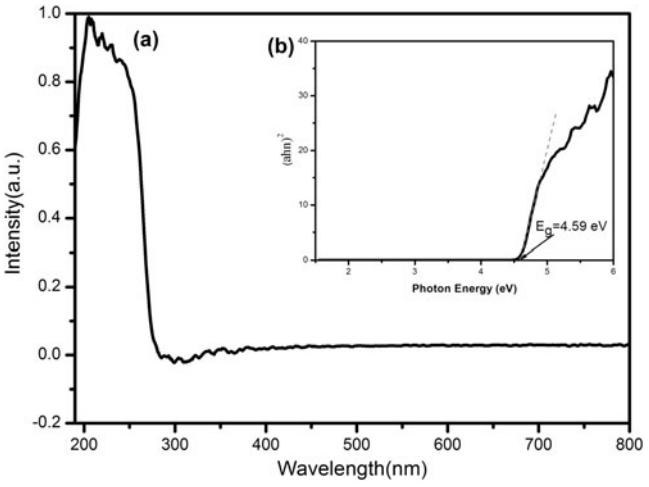


FIG. 3. (a) Absorption spectrum of undoped $Sr_2Ta_2O_7$; (b) $(\alpha h\nu)^2$ versus photon energy $h\nu$.

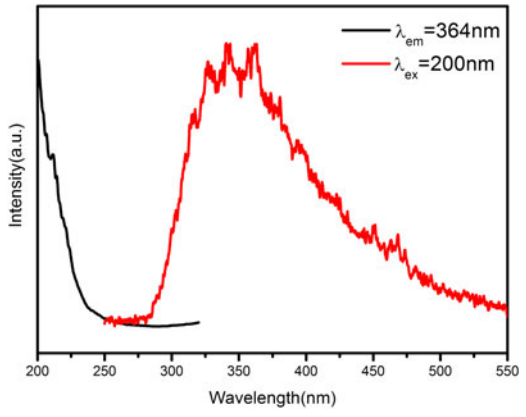


FIG. 4. PL and PLE spectra of pure $Sr_2Ta_2O_7$ (λ_{ex} = 200 nm, λ_{em} = 364 nm).

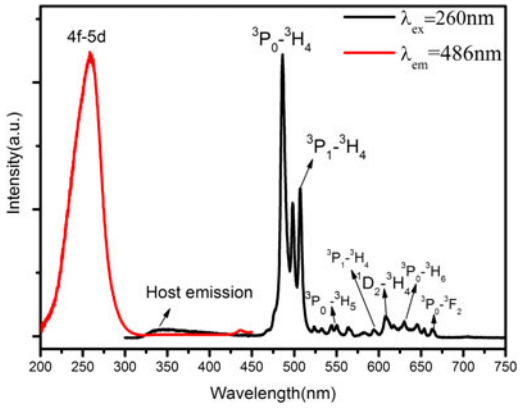


FIG. 5. PL and PLE spectra of the $Sr_2Ta_2O_7$:0.01Pr^{3+} phosphor obtained by solid-state reaction.

https://doi.org/10.1557/jmr.2016.401 Published online by Cambridge University Press

To investigate the concentration quenching effect, the critical distance (R_c) between Pr^{3+} ions can be rough estimated using concentration quenching method proposed by Blasse and Grabmaier as follows[25]:

$$R_c \approx 2\left(\frac{3V}{4\pi x_c N}\right)^{1/3} , \quad (2)$$

where V is the volume of the unit cell, x_c is the critical concentration, and N represents the formula units in the unit cell. In this work, the values of V and N for $Sr_2Ta_2O_7$ are 609.49 $Å^3$ and 4, respectively. And x_c is experimentally to be 0.02 mol. Therefore, the critical distance R_c was calculated to be 24.41 Å.

It is accepted that concentration quenching can be ascribed to energy transfer that include two main aspects: one is the exchange interaction, and the other one is multipolar interaction. It is known that if in the case of the exchange interaction between Pr^{3+} ions, the critical distance between the sensitizer and activator should be shorter than 5 Å. Since the critical distance calculated is considerably greater than 5 Å in the crystalline $Sr_2Ta_2O_7$ host. Consequently, the concentration quenching mechanism may take place by electric multipolar interaction among Pr^{3+} ions.

Thus, the electric multipolar interaction is dominant between Pr^{3+} ions. According to Dexter's energy transfer formula of multipolar interaction, the following equation can be given[26,27]:

$$\frac{I}{X} = \frac{K}{1+\beta(X)^{\theta/3}} . \quad (3)$$

Here, I is the emission intensity, X is the concentration of activator, K and β are constants under the same excitation condition in the same matrix. The value of θ equals to 6, 8, or 10 corresponding to the dipole–dipole, dipole–quadrupole, or quadrupole–quadrupole interactions of the concentration quenching mechanism, respectively. The log(I/X)/log(X) plot was depicted in Fig. 7. The dependence of log(I/X) on log(X) was found to be linear, and the slope of the straight line is −1.96. Thus, the value of θ is found to be very close to 6, which indicates that the dominant concentration quenching mechanism of Pr^{3+} emission in the $Sr_2Ta_2O_7:Pr^{3+}$ phosphor is dipole–dipole interaction.

D. LAG decay characterization of $Sr_2Ta_2O_7:Pr^{3+}$

The afterglow decay curves of samples S1–S5 are presented in Fig. 8. As displayed in Fig. 8, the decay speed was very fast at the initial state, which mainly ascribe to the shallower traps release the carriers with a faster rate, and later a slow decay process was achieved owing to charge carriers in traps with deeper depth released at a slower rate. In this work, the experimental decay curves can be well fitted with a biexponential Eq. (1) as follows:

$$I = I_1 \exp\left(-\frac{t}{\tau_1}\right) + I_2 \exp\left(-\frac{t}{\tau_2}\right) , \quad (4)$$

where I is phosphorescence intensity; I_1 and I_2 are constants; t represents the decay time; τ_1 and τ_2 that determine the rapid and slow decay process, respectively, are decay times for the exponential components. The fitting results are listed in Table I. Obviously, S3 shows the best LAG performance. It can be concluded that the optimal concentration of Pr^{3+} is 0.5 mol% judging from

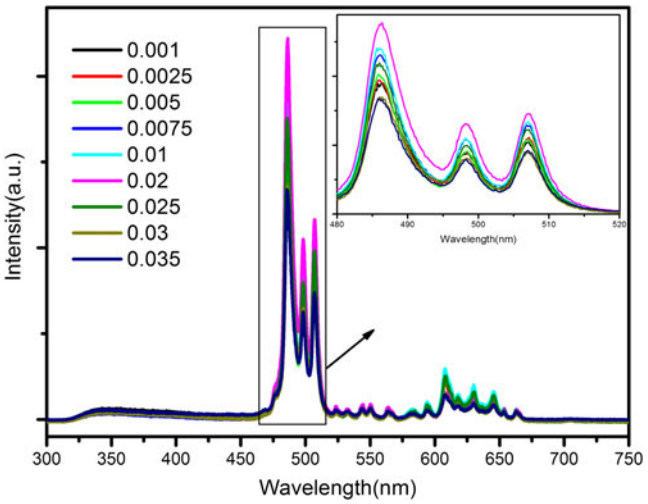


FIG. 6. PL spectra for the $Sr_2Ta_2O_7:xPr^{3+}$ (x = 0.001, 0.0025, 0.005, 0.0075, 0.01, 0.02, 0.025, 0.03, and 0.035) phosphors, and the inset shows enlarged excitation spectra in the range from 480 to 520 nm for samples S1–S9.

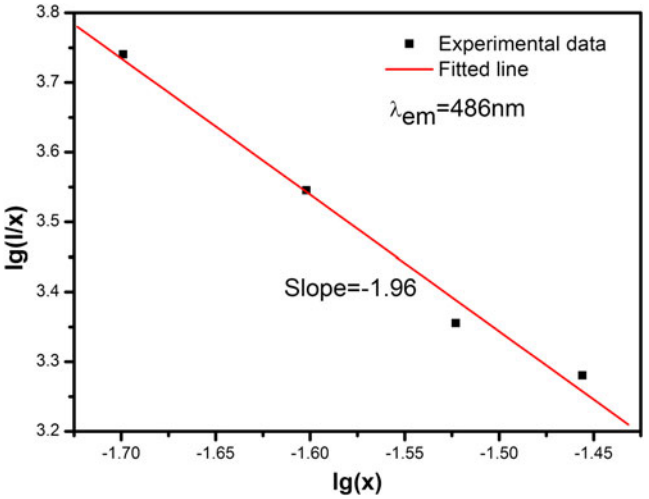


FIG. 7. The dependence of log(I/x) on log(x) based on Eq. (3).

https://doi.org/10.1557/jmr.2016.401 Published online by Cambridge University Press

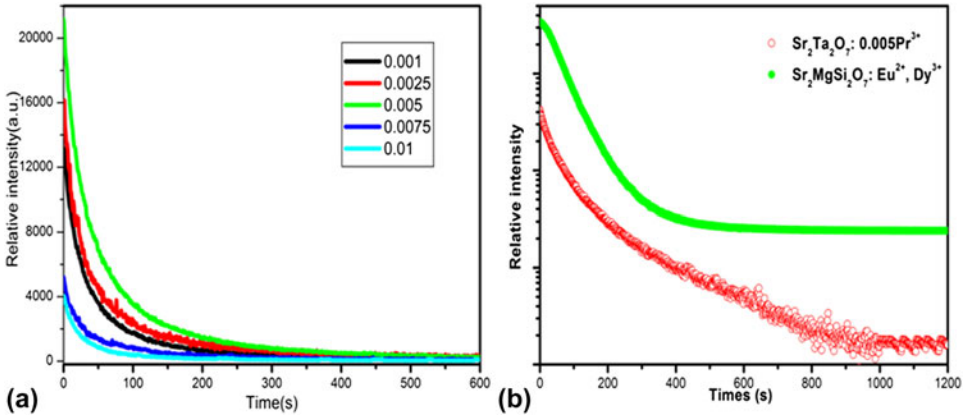


FIG. 8. (a) LAG decay curves for samples S1–S5. (b) The LAG decay curves of $Sr_2Ta_2O_7$:0.005Pr^{3+} and the commercial phosphor $Sr_2MgSi_2O_7$:Eu^{2+},Dy^{3+} in exponential axis.

TABLE I. Simulated result for the afterglow curves of samples S1–S5.

Sample no.	τ_2 (S)	I_1	τ_2 (S)	I_2
S1	18.81	8188	90.09	4675
S2	20.14	9670	96.93	5695
S3	21.97	11,508	98.19	8841
S4	16.49	2946	95.07	1954
S5	15.35	2661	74.09	1280

the highest emission intensity and slowest decay rate. To measure the LAG properties of $Sr_2Ta_2O_7:Pr^{3+}$ phosphor, the comparison with state of the art phosphor $Sr_2MgSi_2O_7:Eu^{2+},Dy^{3+}$ is made. As shown in Fig. 8(b), both the initial brightness of LAG and duration of $Sr_2Ta_2O_7:Pr^{3+}$ cannot be comparable to that of commercial $Sr_2MgSi_2O_7:Eu^{2+},Dy^{3+}$. Indeed, further studies to optimize preparation conditions to improve the initial brightness and duration of this phosphor are under our consideration.

E. TL properties analysis

Theoretically, LAG is attributed to the presence of traps, which are capable of capturing charge carriers (electron or hole trap) under UV-irradiation and then immobilizing these trapped charge carries under thermal disturbance or other physical stimulation for appropriately long time after the removal of UV-irradiation.[28] Generally speaking, LPP with suitable trap depth and high trap density usually exhibit excellent LAG performance. As known, LAG is a temperature-dependent process and traps play an important role in LPP materials. Therefore, to further investigate the trapping centers, TL technique, one of efficient ways to detect some valuable information about the nature of traps, was performed. TL glow curve was often used to analysis of the trap depth and concentration of carriers that are the main determinants of LAG behavior. Typically, the intensity of the TL glow curve is related to the amount of trapped charge carriers, and the maximum temperature of the TL peak provides information on the depth of the charge carriers trap.[29]

The LAG phenomenon can be observed after being irradiated by 200–300 nm wave length. The TL curves of a typical sample $Sr_2Ta_2O_7$:0.001Pr^{3+} at different delay time (t = 30 s, 1, 2, 3, 5, 7, and 10 min) were also recorded to clarify the trap types and completely understand the kinetic processes of traps generated in Pr^{3+}-doped $Sr_2Ta_2O_7$ host. As shown in Fig. 9, it indicates that at least two different kinds of traps with different depths are generated by the incorporation of Pr^{3+} ions because there are two obvious TL peaks. The position of TL peak corresponding to band 1 and band 2 have an obvious shift to high temperature with longer delay time. A reasonable reason is that the trapped electrons/holes escape from shallower traps much faster than those in deep ones. Generally, it is not beneficial for shallow traps to stabilize the charge carriers, which caused extremely short afterglow duration due to the charge carriers escaping too rapidly. Vice versa, the charge carriers in deep depths are very difficult to be released because the activation energy is too high to achieve at room temperature. Empirically, the optimized TL peak is situated slightly above room temperature (320–420 K) for better LAG properties.[30,31]

The TL peak corresponding to band 1 and band 2 are situated ~330 K and ~360 K, respectively. Therefore, two kinds of traps corresponding to two peaks are suitable for the room temperature LAG luminescence. As shown in Fig. 9, the peak intensity of band 1 decreases with a rapid speed, while that of band 2 decreases more slowly. It proves that trapped charge carriers escape from shallower traps much faster than that in deep ones which is consistent with the above. These TL curves with delay time from 3 min to 10 min are analyzed by Chen's peak shape method, which mainly depends on the geometrical form factor

https://doi.org/10.1557/jmr.2016.401 Published online by Cambridge University Press

μ_g [$\mu_g = \frac{\delta}{\omega}$ ($\omega = \delta + \tau$), ω is the full width at half maximum of the TL band, τ is half the width toward low-temperature side, δ is the half width toward high-temperature side]. The values of μ_g with delay time from 3 min to 10 min are calculated about 0.52. Therefore, according to Chen's theory, this case belongs to the second-order kinetic, which means the possibility that electrons once released from traps may be retrapped by traps. To sum up, the trap depth and trap density of TL glow curves for different delay times (3–10 min) of $Sr_2Ta_2O_7$:0.001Pr^{3+} samples can be roughly calculated according to the following two Eqs. (5) and (6), respectively:[32,33]

$$E = 3.5\left(\frac{k_B T_m^2}{\omega}\right) - 2k_B T_m \quad , \tag{5}$$

$$n_0 = \frac{\omega I_m}{\beta\left[2.52 + 10.2\left(\mu_g - 0.42\right)\right]} \quad . \tag{6}$$

In Eq. (5), E is the trap depth; k_B is Boltzmann's constant; T_m is the temperature (in Kelvin) corresponding to the TL glow peak. In Eq. (6), n_0 is the trap density, I_m is the TL intensity of each glow peak and β is the heating rate (1 K/s). The calculated values of E and n_0 are presented in Table II. For TL band 2, the trap depth becomes deeper with longer delay time. It may be caused by release of charge carriers from trap centers. Furthermore, it can also be proved from the trap density decrease with the increase of delay time. Obviously, the value of $t = 3$ min is much smaller than that of $t > 3$ min, which is mainly because the peak is formed by overlapping band 1 and band 2 and the contribution of band 1 is quite large.

Furthermore, to better study the band 2 and avoid the impact of band 1, the TL curves of samples S1–S5 were recorded after being preheated at 70 °C for 5 min. The glow curves of samples S1–S5 are illustrated in Fig. 10. These TL curves with different concentration are analyzed by the same method as mentioned above. The calculated values of E and n_0 are presented in Table III. It can be seen that the trap depth corresponding to different samples are about 0.98 eV. The trap density approaches the maximum at $x = 0.5$ mol%.

IV. MECHANISM OF LAG IN $Sr_2Ta_2O_7$:Pr^{3+}

At the moment, the origin of the defects needs further studies to further investigate the mechanism of LAG in Pr^{3+}-doped $Sr_2Ta_2O_7$. The generation of defects may be caused by two aspects: firstly, the intrinsic defects (e.g., strontium, tantalum, and oxide vacancies created by the

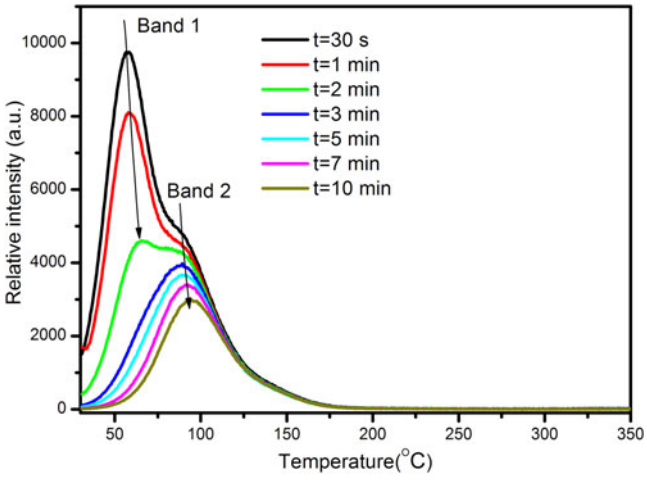


FIG. 9. TL glow curves of sample $Sr_2Ta_2O_7$:0.001Pr^{3+} at different delay times (t = 30 s, 1, 2, 3, 5, 7, and 10 min).

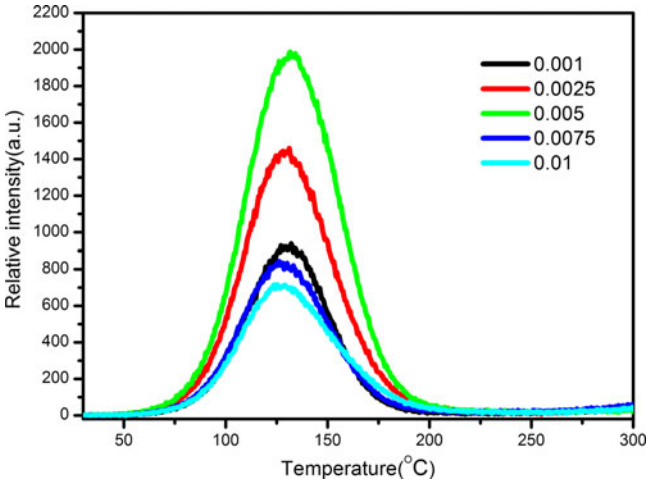


FIG. 10. TL curves of samples S1–S5.

TABLE II. Estimated trap depths (E) and densities (n_0) of sample S1 with different delay times.

	Band 2 parameters		
Delay time	T_m (K)	E (eV)	$n_0 \times 10^4$ $(cm^3)^{-1}$
3 min	362	0.703	7.048
5 min	363	0.758	4.963
7 min	365	0.822	3.921
10 min	368	0.869	3.465

TABLE III. Estimated trap depths (E) and densities (n_0) of samples S1–S5.

	Parameters		
Sample no.	T_m (K)	E (eV)	$n_0 \times 10^4$ $(cm^3)^{-1}$
S1	401	0.979	1.412
S2	401	0.98	1.875
S3	404	0.983	2.991
S4	402	0.967	1.301
S5	401	0.978	1.043

https://doi.org/10.1557/jmr.2016.401 Published online by Cambridge University Press

evaporation of Sr or Ta in the reaction process at high temperature). $[V_{Sr^{2+}}]''$ and $[V_{Ta^{5+}}]'''''$ can serve as hole trap centers. And the oxygen vacancies $[V_O]$ which are generated for charge compensation can be regarded as electron trap centers. Secondly, charge compensation defects related to the presence of Pr^{3+} substituted Sr^{2+} sites and produced defects via the process $2Pr^{3+} + 3Sr^{2+} \rightarrow 2[Pr^{3+}_{Sr^{2+}}]^{\bullet} + [V_{Sr^{2+}}]''$ in $Sr_2Ta_2O_7$ host lattice. The defects $[Pr^{3+}_{Sr^{2+}}]^{\bullet}$ can act as electron traps.

To understand the LAG of Pr^{3+}-doped $Sr_2Ta_2O_7$ or Pr^{3+}-doped any host, the entire mechanism must be constructed. Based entirely on the above descriptions and analysis, a possible mechanism of LAG in Pr^{3+}-doped $Sr_2Ta_2O_7$ can be proposed and intended to explain the LAG phenomenon. As illustrated in Fig. 11. On the one hand, under UV excitation (200–300 nm), electrons in ground state $^3H_4$ are excited into $4f^15d$ states (process numbered ①). On the other hand, electrons can be excited directly from valence band into conduction band (process ②). The majorities of excited electrons will move to $^3P_2$ level and then they will relax to $^3P_1$, $^3P_0$, $^1D_2$ levels with nonradiation relaxation (process ③). Subsequently, the electrons jumping from $^3P_1$, $^3P_0$, and $^1D_2$ levels to ground levels of ^3H_j (j = 6, 5, and 4) results in the characteristic emission of Pr^{3+} ions (process ④). Meanwhile, part of excited electrons can be captured by shallower traps rather than the process mentioned above, then be captured by deep traps through tunneling (process ⑤). Therefore, after cutting off the ultraviolet light, those charge carriers (electrons or holes) trapped in shallower traps can be released gradually from the trapping centers with rapid speed, while the those in deep traps can be released with slow speed (process numbered ⑥). Then the motion process as that described in PL occurs, which leads to the characteristic emission of Pr^{3+} ions as blue emissive LAG. Finally, the motion process of recombination between electrons and holes occurs (process numbered ⑦).

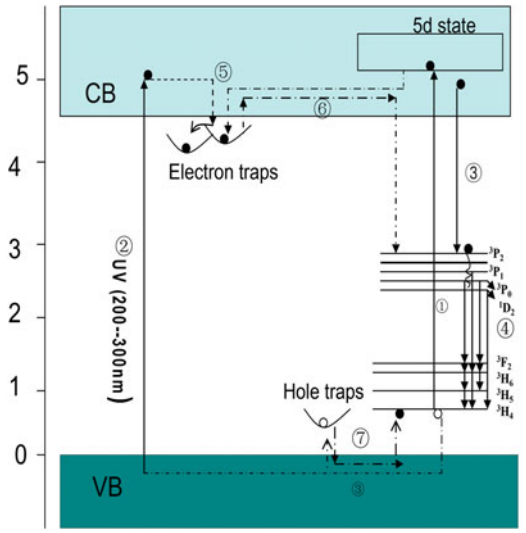


FIG. 11. A schematic diagram of LAG mechanism for $Sr_2Ta_2O_7:Pr^{3+}$.

V. CONCLUSION

In summary, the novel blue emitting Pr^{3+}-doped $Sr_2Ta_2O_7$ phosphors with persistent emission properties were synthesized successfully through a solid-state reaction. The blue LAG phenomenon was observed after being excited by UV-light. The mechanism of concentration quenching is studied systematically. The optimal Pr^{3+}-doping concentration for the best photoluminescence and LAG properties were experimentally to be 2 mol% and 0.5 mol%, respectively. Furthermore, to explain the motion of charge carriers and clarify the generation mechanism, a simplified model for the illustration of LAG mechanism was also proposed.

ACKNOWLEDGMENT

The authors acknowledge the financial support from the National Natural Science Foundation of China (No. 21471038).

REFERENCES

1. A. Bessière, S.K. Sharma, N. Basavaraju, K.R. Priolkar, L. Binet, B. Viana, A.J.J. Bos, T. Maldiney, C. Richard, D. Scherman, and D. Gourier: Storage of visible light for long-lasting phosphorescence in chromium-doped zinc gallate. *Chem. Mater.* **26**, 1365 (2014).
2. L. Jin, H. Zhang, R. Pan, R. Pan, P. Xu, J. Han, X. Zhang, Q. Yuan, Z. Zhang, X. Wang, Y. Wang, and B. Song: Observation of the long afterglow in AlN helices. *Nano Lett.* **15**, 6575 (2015).
3. T. Matsuzawa, Y. Aoki, N. Takeuchi, and Y. Murayama: A new long phosphorescent phosphor with high brightness, $SrAl_2O_4$: Eu^{2+},Dy^{3+}. *J. Electrochem. Soc.* **143**, 2670 (1996).
4. F.Q. Sun, R.R. Xie, L. Guan, and C.Y. Zhang: The near-infrared long-persistent phosphorescence of Cr^{3+}-activated non-gallate phosphor. *Mater. Lett.* **164**, 39 (2016).
5. R.L. Nyenge, H.C. Swart, D. Poelman, P.F. Smetc, L.I.D.J. Martinc, L.L. Notoa, S. Som, and O.M. Ntwaeaborwaa: Thermal quenching, cathodoluminescence and thermoluminescence study of Eu^{2+} doped CaS powder. *J. Alloys Compd.* **657**, 787 (2016).
6. B. Liu, C. Shi, M. Yin, L. Dong, and Z.G. Xia: The trap states in the $Sr_2MgSi_2O_7$ and $(Sr, Ca)_2MgSi_2O_7$ long afterglow phosphor activated by Eu^{2+} and Dy^{3+}. *J. Alloys Compd.* **387**, 65 (2005).
7. J. Hölsä: Persistent luminescence beats the afterglow: 400 years of persistent luminescence. *Electrochem. Soc. Interface* **18**, 42 (2009).
8. Z. Pan, Y.Y. Lu, and F. Liu: Sunlight-activated long-persistent luminescence in the near-infrared from Cr^{3+}-doped zinc gallogermanates. *Nat. Mater.* **11**, 58 (2012).
9. M. Allix, S. Chenu, E. Véron, E. Véron, T. Poumeyrol, E.A. Kouadri-Boudjelthia, S. Alahraché, F. Porcher, D. Massiot, and F. Fayon: Considerable improvement of long-persistent luminescence in germanium and tin substituted $ZnGa_2O_4$. *Chem. Mater.* **25**, 1600 (2013).

https://doi.org/10.1557/jmr.2016.401 Published online by Cambridge University Press

10. Z. Fu, S. Zhou, and S. Zhang: Study on optical properties of rare-earth ions in nanocrystalline monoclinic $SrAl_2O_4$:Ln (Ln = Ce^{3+}, Pr^{3+}, Tb^{3+}). *J. Phys. Chem. B* **109**, 14396 (2005).
11. Z.L. Hong, P.Y. Zhang, X.P. Fan, and Q.M. Wang: Eu^{3+} red long afterglow in Y_2O_2S:Ti, Eu phosphor through afterglow energy transfer. *J. Lumin.* **124**, 127 (2007).
12. E.G. Yukihara and S.W.S. McKeever: *Optically stimulated luminescence: Fundamentals and applications*, 1st ed. (John Wiley & Sons, Hoboken, 2011).
13. Z.M. Qi, C.S. Shi, M. Liu, D.F. Zhou, X.X. Luo, J. Zhang, and Y.N. Xie: The valence of rare earth ions in $R_2MgSi_2O_7:Eu^{2+},Dy^{3+}$ (R = Ca, Sr) long-afterglow phosphors. *Phys. Status Solidi A* **201**, 3109 (2004).
14. X.M. Zhang, H. Chen, W.J. Ding, H. Wu, and J. Kim: $Ca_2B_5O_9Cl:Eu^{2+}$, a suitable blue-emitting phosphor for n-UV excited solid-state lighting. *J. Am. Ceram. Soc.* **92**, 429 (2009).
15. F.W. Kang, Y. Zhang, L. Wondraczek, J.Q. Zhu, X.B. Yang, and M.Y. Peng: Processing-dependence and the nature of the blue-shift of Bi^{3+}-related photoemission in $ScVO_4$ at elevated temperatures. *J. Mater. Chem. C* **2**, 9850 (2014).
16. F.W. Kang, X.B. Yang, M.Y. Peng, L. Wondraczek, Z.J. Ma, Q.Y. Zhang, J.R. Qiu: Red photoluminescence from Bi^{3+} and the influence of the oxygen-vacancy perturbation in $ScVO_4$: A combined experimental and theoretical study. *J. Phys. Chem. C* **118**, 7517 (2014).
17. L. Zhang and Y. Zhu: A review of controllable synthesis and enhancement of performances of bismuth tungstate visible-light-driven photocatalysts. *Catal. Sci. Technol.* **2**, 694 (2012).
18. Y.G. Su, L.M. Peng, J.W. Guo, S.S. Huang, L. Lv, and X.J. Wang: Tunable optical and photocatalytic performance promoted by nonstoichiometric control and site-selective codoping of trivalent ions in $NaTaO_3$. *J. Phys. Chem. C* **118**, 10728 (2014).
19. L.L. Noto, M.Y.A. Yagoub, O.M. Ntwaeaborwa, and H.C. Swart: Persistent photoluminescence emission from $SrTa_2O_6:Pr^{3+}$ phosphor prepared at different temperatures. *Ceram. Int.* **41**, 8828 (2015).
20. P. Liu, J. Nisar, R. Ahuja, and B. Pathak: Layered perovskite $Sr_2Ta_2O_7$ for visible light photocatalysis: A first principles study. *J. Phys. Chem. C* **117**, 5043 (2013).
21. A. Mukherji, B. Seger, G.Q. Lu, et al.: Nitrogen doped $Sr_2Ta_2O_7$ coupled with graphene sheets as photocatalysts for increased photocatalytic hydrogen production. *ACS Nano* **5**, 3483 (2011).
22. N. Ishizawa, F. Marumo, T. Kawamura, and M. Kimura: Compounds with perovskite-type slabs. II. The crystal structure of $Sr_2Ta_2O_7$. *Acta Crystallogr., Sect. B: Struct. Crystallogr. Cryst. Chem.* **32**, 2564 (1976).
23. N. Ishizawa, F. Marumo, and S. Iwai: Compounds with perovskite-type slabs. IV. Ferroelectric phase transitions in $Sr_2(Ta_{1-x}Nb_x)_2O_7$ ($x \simeq 0.12$) and $Sr_2Ta_2O_7$. *Acta Crystallogr., Sect. B: Struct. Crystallogr. Cryst. Chem.* **37**, 28 (1981).
24. L.L. Noto, M.L. Chithambo, O.M. Ntwaeaborwa, and H.C. Swart: The greenish-blue emission and thermoluminescent properties of $CaTa_2O_6:Pr^{3+}$. *J. Alloys Compd.* **589**, 91 (2014).
25. G. Blasse: Energy transfer in oxidic phosphors. *Phys. Lett. A* **28**, 444 (1968).
26. D.L. Dexter and J.H. Schulman: Theory of concentration quenching in inorganic phosphor. *J. Chem. Phys.* **22**, 1063 (1954).
27. L. Ozawa and P.M. Jaffe: The mechanism of the emission color shift with activator concentration in +3 activated phosphors. *J. Electrochem. Soc.* **118**, 1679 (1971).
28. G.B. Che, C.B. Liu, X.Y. Li, Z.L. Xu, Y. Liu, and H. Wang: Luminescence properties of a new Mn^{2+}-activated red long-afterglow phosphor. *J. Phys. Chem. Solids.* **69**, 2091 (2008).
29. H.J. Guo, Y.H. Wang, W.B. Chen, W. Zeng, S.C. Han, G. Li, and Y.Y. Li: Controlling and revealing the trap distributions of $Ca_6BaP_4O_{17}:Eu^{2+},R^{3+}$ (R = Dy, Tb, Ce, Gd, Nd) by codoping different trivalent lanthanides. *J. Mater. Chem. C* **3**, 11216 (2015).
30. J. Trojan-Piegza, J. Niittykoski, J. Hölsä, and E. Zych: Thermoluminescence and kinetics of persistent luminescence of vacuum-sintered Tb^{3+}-doped and Tb^{3+}, Ca^{2+}-codoped Lu_2O_3 materials. *Chem. Mater.* **20**, 2258 (2008).
31. X. Sun, J. Zhang, X. Zhang, Y. Luo, and X.J. Wang: Long lasting yellow phosphorescence and photostimulated luminescence in $Sr_3SiO_5:Eu^{2+}$ and $Sr_3SiO_5:Eu^{2+},Dy^{3+}$ phosphors. *J. Phys. D: Appl. Phys.* **41**, 195414 (2008).
32. R. Chen: On the calculation of activation energies and frequency factors from glow curves. *J. Appl. Phys.* **40**, 580 (1969).
33. R. Chen: Glow curves with general order kinetics. *J. Electrochem. Soc.* **116**, 1254 (1969).

https://doi.org/10.1557/jmr.2016.401 Published online by Cambridge University Press